Crystal, Magnetic Structures, and Bonding Interactions in the TiNiSi-Type Hydride CeMgSnH

Experimental and Computational Studies

Yartys, Volodymyr A.; Akselrud, Lev G.; Denys, Roman V.; Vajeeston, Ponniah; Ouladdiaf, Bachir; Dankelman, Robert; Plomp, Jeroen; Kremer, Reinhard K.; Pöttgen, Rainer; More Authors

DOI
10.1021/acs.chemmater.4c01104

Publication date
2024

Document Version
Final published version

Published in
Chemistry of Materials

Citation (APA)
Yartys, V. A., Akselrud, L. G., Denys, R. V., Vajeeston, P., Ouladdiaf, B., Dankelman, R., Plomp, J., Kremer, R. K., Pöttgen, R., & More Authors (2024). Crystal, Magnetic Structures, and Bonding Interactions in the TiNiSi-Type Hydride CeMgSnH: Experimental and Computational Studies. *Chemistry of Materials*, *36*(12), 6257-6268. https://doi.org/10.1021/acs.chemmater.4c01104

CHEMISTRY OF MATERIALS

pubs.acs.org/cm

Article

Crystal, Magnetic Structures, and Bonding Interactions in the TiNiSi-Type Hydride CeMgSnH: Experimental and Computational Studies

Published as part of Chemistry of Materials virtual special issue "In Memory of Prof. Francis DiSalvo".

Volodymyr A. Yartys,* Lev G. Akselrud, Roman V. Denys, Ponniah Vajeeston, Bachir Ouladdiaf, Robert Dankelman, Jeroen Plomp, Aylin Koldemir, Lars Schumacher, Reinhard K. Kremer,* Rainer Pöttgen,* David S. Wragg, Bruno Guilherme Fischer Eggert, and Vasyl Berezovets

Cite This: *Chem. Mater.* 2024, 36, 6257−6268

Read Online

ACCESS | Metrics & More | Article Recommendations | Supporting Information

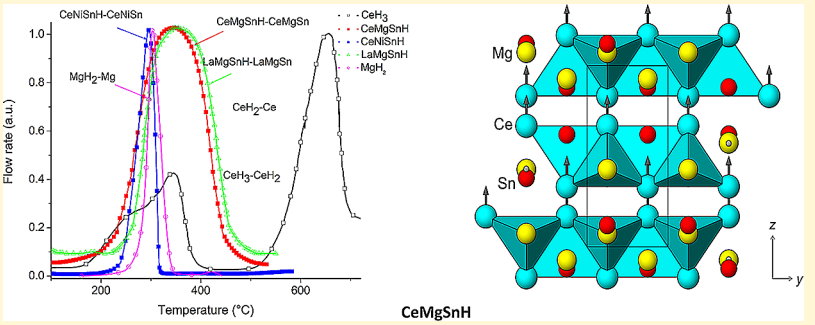

ABSTRACT: By combining experimental and computational studies, the orthorhombic stannide CeMgSn with a TiNiSi-type structure has been characterized as a potential hydrogen storage material. Experimental studies of the formed monohydride CeMgSnH including hydrogen absorption−desorption, thermal desorption spectroscopy, synchrotron and neutron powder diffraction (298 and 2 K), magnetization, and ^{119}Sn Mössbauer spectroscopic measurements are discussed in parallel with ab initio electronic structure calculations. A small, 1.27 vol %, expansion of the unit cell of CeMgSn during its transformation into a thermally stable CeMgSnH monohydride is caused by an ordered insertion of H atoms into half of the available Ce_3Mg tetrahedral interstices leaving the $CeMg_3$ tetrahedra unoccupied. The bonding in CeMgSnH is dominated by strong Ce−Sn and Mg−Sn interactions which are almost not altered by hydrogenation, whereas the H atoms carry a small negative charge and show bonding interactions with Ce and Mg. Hydrogenation causes a conversion of the antiferromagnetic CeMgSn into ferromagnetic CeMgSnH with the Ce moments aligned along [001] with a magnetic moment of 1.4(3) μ_B. The ^{119}Sn isomer shifts and the values of quadrupole splitting in the Mössbauer spectra suggest a similar *s*-electron density distribution for the Ce- and La-containing REMgSnH monohydrides.

1. INTRODUCTION

In the large family of rare earth intermetallic compounds, cerium-based ones play an important role. This is directly related to the peculiar electronic situation of the cerium atoms, allowing for trivalent paramagnetic cerium with a [Xe] $4f^1$ configuration and tetravalent diamagnetic cerium with an empty f shell. In between, many intermediate-valent cerium intermetallics have been observed. The many crystal-chemical data are summarized in the Pearson database.[1] An overview on the manifold of physical properties, especially the magnetic behavior, is given in the Szytuła Handbook.[2]

The important parameter that governs the magnetic ground state of an intermetallic cerium compound is the coupling constant J_{cf} between the Ce(4f) and conduction electrons. Indirect RKKY interactions and the Kondo effect are the competing parameters.

Theoretical studies of the hydrides of ternary cerium-based intermetallics showed that a competition between these two opposite effects results in a variety of physical properties caused by the differences in the electronic state of Ce, including intermediate valence cerium, magnetic Kondo compounds, heavy Fermions' systems, spin glass, and BCS superconductors.[3] These changes are caused by charge transfer to H atoms and by the volume expansion effect because of the insertion of hydrogen atoms into the metal substructure.

Received: April 15, 2024
Revised: June 5, 2024
Accepted: June 5, 2024
Published: June 13, 2024

Earlier studied $CeMg_2H_7$ hydride has the highest H/M ratio for the hydrides of Laves phases, 6.33.[4] The hydrogen (deuterium) distribution consists of four symmetry-independent, fully occupied sites having triangular Ce_2Mg and tetrahedral Ce_2Mg_2 and Mg_4 metal coordinations with distances in the ranges of Ce−D = 2.36−2.51 Å and Mg−D = 1.91−2.18 Å. Interestingly, $CeMg_2$ does not disproportionate into MgH_2 and CeH_3 even when subjected to the H_2 pressure of 50 bar H_2 at 100 °C and instead forms $CeMg_2H_7$.[4] This can be related to the bonding interactions between Ce and Mg atoms which were theoretically studied in ref 5 which prevents such a disproportionation.

The equiatomic CeTX intermetallic compounds with T = transition metal and X = Sn or another main-group element play an important role in showing interesting properties. Depending on the element combination and the valence electron concentration (VEC), the CeTX phases crystallize with a large variety (more than 30) of different structure types.[6,7] These phases have attracted significant interest in solid-state chemistry and physics with respect to their broadly varying physical properties. The orthorhombic TiNiSi-type structural family belongs to the two most abundant types of the CeTX intermetallics including many of the CeTSn stannides.[6,7] Modification of the electronic structure and thus the magnetic ground state of CeTX intermetallics is possible under high-pressure conditions and most effectively upon hydrogenation.

The CeTX intermetallics with a TiNiSi-type structure form stable mono- and dihydrides with different magnetic properties: CeNiSnH is an antiferromagnet (AFM) with the Ce magnetic moment of 1.37(3) μ_B/Ce along [001] for the setting in space group $Pna2_1$.[8] $CeNiSnH_{1.8}$ is ferromagnetic (FM) with a Ce moment of 1.28 μ_B/Ce aligned along [001].[9] $CeNiGaH_{1.1}$ exhibits no long-range magnetic order.[10] CePdSnH is an AFM with a moment of 2.74(2) μ_B/Ce (powder data),[11] and $CeRhSbH_{0.2}$ is an AFM with a moment of 0.19 μ_B/Ce.[12] The hydride formation is accompanied by a small volume expansion, not exceeding 3 vol %, associated with an insertion of H atoms into Ce_3T tetrahedral voids as it was verified by a neutron powder diffraction study of CeNiSnD.[8]

Hydrogenation causes various changes in the magnetic properties, which can be related to the valence state of cerium. One example is the Kondo semimetal CeNiSn where the hydrogenation induces antiferromagnetism in CeNiSnH,[8] whereas the dihydride $CeNiSnH_{1.8}$[9] shows ferromagnetism.

The highest hydrogen storage capacity for the RETSn (RE = rare earth metal) stannides has been observed for the hydride $LaNiSnH_2$,[13] containing two H atoms/f.u. of RETSn. During hydrogenation, its crystal structure transforms from an orthorhombic TiNiSi to the closely related hexagonal ZrBeSi type with the H atoms filling all available La_3Ni tetrahedral interstices. Both structures derive from aristotype AlB_2.

Substitution of Ni by Mg in LaNiSn results in the formation of an orthorhombic LaMgSn. Compared to LaNiSn, the crystal structure of LaMgSn is significantly expanded by 17 vol % because of the replacement of smaller Ni atoms by the much larger Mg atoms. Hydrogenation of LaMgSn to the monohydride LaMgSnH, space group *Pnma*; a = 8.1628(4) Å; b = 4.5555(3) Å; c = 9.2391(5) Å; (V_{cell} = 343.56(5) Å^3) causes a small (1.26%) increase of the unit cell volume with the expansion mainly along the [100] direction. Hydrogen absorption−desorption cycles in vacuum resulted in a reversible formation of the initial compound LaMgSn, with the peak of hydrogen release occurring at 355 °C. Deuterium atoms completely fill half of the available La_3Mg interstitial sites in an ordered manner with metal-H/D distances of Mg-D = 2.026 Å; La-D = 2.381; and 2.502 Å. ^{119}Sn Mössbauer spectra of paramagnetic LaMgSn and LaMgSnH showed isomer shifts of 1.98(2) and 1.99(1) mm/s, respectively, typical for the crystal chemically similar RETSn stannides.[14]

Also, CeMgSn crystallizes with a TiNiSi-type structure. It is chemically related to LaMgSn. However, as the Ce atoms carry magnetic moments, CeMgSn shows long-range magnetic order with predominantly antiferromagnetic interactions.[15,16]

The present investigation was aimed at the hydrogenation behavior and the effect of hydrogen insertion on the crystal and magnetic structures of CeMgSnH. We have studied hydrogen absorption−desorption by thermal desorption spectroscopy (TDS), synchrotron X-ray diffraction (SR XRD), and neutron powder diffraction (NPD) characterization of the deuterated samples at 2 and 298 K, magnetization measurements, ^{119}Sn Mössbauer spectroscopy, and density functional theory (DFT) computational studies of the electronic structure and chemical bonding.

2. EXPERIMENTAL DETAILS

2.1. Initial Intermetallic Compound. CeMgSn was prepared from a mixture of Mg and an arc-melted CeSn precursor (the purity of the initial metals was better than 99.9 wt %). Mixtures of the constituents were milled together and pressed into pellets at 25 MPa. An excess of 4 wt % of Mg was added as compared to the stoichiometric 1:1 mixture of Mg and CeSn to compensate for the sublimation of magnesium during the high-temperature synthesis. The pellets were wrapped in tantalum foil and placed into stainless steel tubes. The tubes were sealed by welding in an Ar atmosphere, annealed at 800 °C for 24 h, and subsequently quenched into a water-ice bath. X-ray diffraction (XRD) studies were performed on a Bruker D2 Phaser diffractometer by using monochromatic Cu Kα radiation.

2.2. Synthesis of Hydride/Deuteride. The hydrogenation/deuteration reaction of CeMgSn was performed at 200 °C and 20 bar H_2/D_2 after a heat treatment of the starting material in dynamic vacuum at 350 °C. The absorption of hydrogen/deuterium typically lasted for about 3 h, but to ensure complete hydrogenation, the sample was kept under the reaction conditions for 24 h. The hydrogen/deuterium content was determined from the change of the gas pressure in a calibrated volume. Approximately 2.0 g of CeMgSn was used for the preparation of the deuteride, subsequently characterized by neutron powder diffraction (NPD). Purity of the deuterium gas was better than 99.9%. CeMgSn and CeMgSnH are moisture-sensitive and were handled and kept under inert conditions.

2.3. Thermal Desorption Spectroscopy. TDS spectra were collected at a heating rate of 2 K/min in a temperature interval of 20−550 °C. Approximately 300 mg of the samples was loaded in an Ar glovebox into an autoclave made of a 1/2″ SS316 stainless steel tubing, equipped with a port for a K-type thermocouple. Before TDS was started, the pressure in the autoclave was better than 1×10^{-5} mbar. The gas evolution was monitored by the pressure at the entrance of the turbomolecular pump measured with a Pirani−Penning vacuum gauge and found between 3×10^{-5} and 2×10^{-2} mbar. Further calibration allowed us to quantitatively determine the H_2 desorption flow (N cm^3 min^{-1} g^{-1}) from the pressure gauge reading. The TDS measurements were performed with a temperature sequence described earlier.[17]

2.4. Synchrotron and Neutron Powder Diffraction Studies. XRD examination of the samples was performed using a Bruker D2 Phaser diffractometer with Cu Kα (λ = 1.5406 Å) radiation in Bragg−Brentano geometry and showed the formation of a high-purity TiNiSi-type intermetallic compound. SR XRD patterns of CeMgSn and CeMgSnH were collected at beamline BM01, SNBL, ESRF, Grenoble, France, using a wavelength of 0.75334 Å. The powdered

https://doi.org/10.1021/acs.chemmater.4c01104
Chem. Mater. 2024, 36, 6257−6268

samples were sealed in ~0.3 mm glass capillaries. The instrument used to collect the data and the azimuthal integration method used on the 2D detector images are described in ref 18. The refinements of the SXRD data of CeMgSn intermetallic yielded the unit cell parameters of a = 7.73761(8); b = 4.65018(4); c = 9.08842(9) Å; V = 343.56(5) Å^3 which agree well with the reference data (see the Supporting Information file for further details on the crystal structure data).

NPD patterns were collected at the 2 MW research reactor of Delft University of Technology (the Netherlands) using the PEARL diffractometer[19] and a wavelength of 1.67 Å obtained with a Ge monochromator. The powdered sample, ~2 g, was hermetically sealed in a vanadium can (outer diameter, 6 mm). Powder diffraction patterns were collected at 298 K and on cooling to 2 K using an orange ILL cryostat. The refinements of the SXRD and NPD pattern were performed using the WinCSD and the FullProf software packages.[20,21]

2.5. Magnetization Measurements. Magnetic susceptibilities of polycrystalline samples of CeMgSn and CeMgSnD as a function of the temperature were measured at magnetic fields between 0.1 and 7 T with an MPMS X7 SQUID magnetometer (Quantum Design). The samples were sealed in quartz glass tubes, the magnetizations of which were determined in separate runs and subtracted.

Isothermal magnetization data $M(T, H)$ of CeMgSn and CeMgSnD were measured in the temperature range of 1.8−300 K and in magnetic fields up to 90 kOe with the vibrating sample magnetometer (VSM) option of a physical property measurement system (DynaCool PPMS) by Quantum Design. The sample powders were filled into polypropylene capsules and attached to a sample holder rod. Fitting and plotting the data were done with OriginPro 2021b[22] and the graphical editing with the program CorelDraw 2017.[23]

2.6. ^{119}Sn Mössbauer Spectroscopy. A $Ca^{119m}SnO_3$ γ-source was used in the standard transmission geometry. The CeMgSn and CeMgSnD samples were investigated at T = 78 K in a commercial liquid nitrogen bath cryostat. The source was kept at room temperature. The samples were prepared by mixing with α-quartz and placed in thin-walled PMMA containers. The optimal absorber thickness was calculated according to the work of Long et al.[24] The spectra were fitted with the WinNormos for Igor7 software package,[25] and the graphical editing was performed with the program CorelDRAW2017.[23]

2.7. Theoretical Studies of the Electronic Structures. Total energies were computed using the projector augmented plane wave (APW) implementation within the Vienna ab initio simulation package (VASP).[26−32] The Perdew, Burke, and Ernzerhof (PBE) exchange−correlation functional[30] augmented by Hubbard parameter corrections (GGA+U) was employed for these calculations, with Ce-f states parametrized using U values set at 5.1 and J at 1 eV. The interaction of the core and valence electrons was considered using the projector augmented wave (PAW) method.[31,32] Ground-state geometries were determined through stress and Hellmann−Feynman force minimization by utilizing the conjugate gradient algorithm with a force convergence threshold of less than 10^{-3} eV Å^{-1}.

During all relaxation procedures, the Brillouin zone integration was performed employing a Gaussian broadening of 0.1 eV. Our analysis indicated that a 1280 k-point mesh uniformly distributed across the entire Brillouin zone and a 600 eV plane wave cutoff ensured optimal accuracy for the calculated results. These k-points were generated using the Monkhorst−Pack method with a 10 × 16 × 8 grid for structural optimization. A commensurate k-point density and energy cutoff were applied to determine the total energy as a function of volume for all considered structures. The iterative relaxation of atomic positions was terminated when the change in total energy between consecutive steps was less than 1 meV per cell, ensuring convergence to the ground-state configuration with high precision.

3. RESULTS

3.1. Stannide CeMgSn. Rietveld powder refinements of the SR XRD pattern of CeMgSn assured an excellent quality of the sample and confirmed a single-phase intermetallic compound with a TiNiSi-type orthorhombic structure with the unit cell parameters: space group $Pnma$ (No. 62); a = 7.73761(8); b = 4.65018(4); c = 9.08842(9) Å; V = 327.013(5) Å^3 (see Figure 1). These data agree well with the reference data.[15] The full set of crystallographic data for CeMgSn is given in Table S1 with interatomic distances Ce−Ce, Ce−Mg, and Mg−Sn listed in Table S2 of the Supporting Information file.

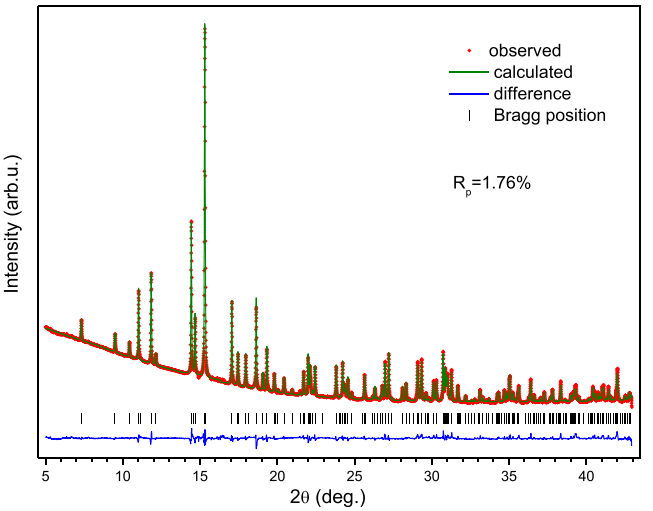

Figure 1. SR XRD powder diffraction pattern of CeMgSn collected using the multipurpose diffractometer at BM01, SNBL, ESRF, Grenoble, France, using a wavelength of 0.75334 Å. R_{prof} = 0.0176. The vertical bars at the bottom and the blue line indicate the angles of the Bragg reflections used to simulate the refined pattern and the difference between the measured and refined patterns, respectively.

3.2. Thermal Desorption Spectroscopy Study of CeMgSnH. Hydrogen desorption proceeds in a broad temperature range peaking at 345 °C (Figure 2) similarly to

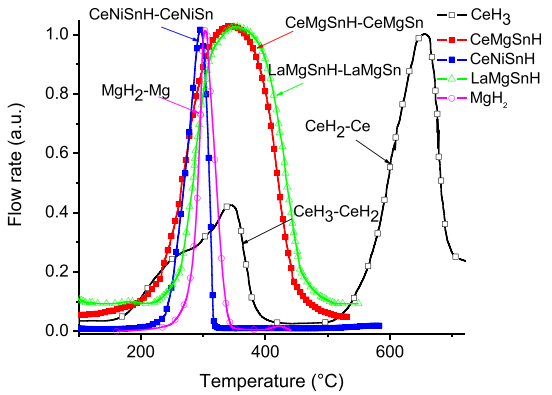

Figure 2. Thermal desorption spectrum of the CeMgSnH hydride (2 K/min) shown in comparison with TDS traces for CeNiSnH (this work), $LaNiSnH_2$ (adopted from ref 13), LaMgSnH (adopted from ref 14), and CeH_3 (adopted from ref 33). The peak temperatures (in °C) depend on the chemical composition of the hydrides and on the surroundings of the interstices associated with hydrogen desorption as follows: CeNiSnH−CeNiSn, 295 (H in Ce_3Ni tetrahedra); MgH_2−Mg, 302 (H in Mg_4 tetrahedra); CeH_3−CeH_2, 344 (H in Ce_6 octahedra); CeMgSnH−CeMgSn, 345 (H in Ce_3Mg tetrahedra); LaMgSnH−LaMgSn, 354 (H in La_3Mg tetrahedra); CeH_2−Ce, 655 (H in Ce_4 tetrahedra).

https://doi.org/10.1021/acs.chemmater.4c01104
Chem. Mater. 2024, 36, 6257−6268

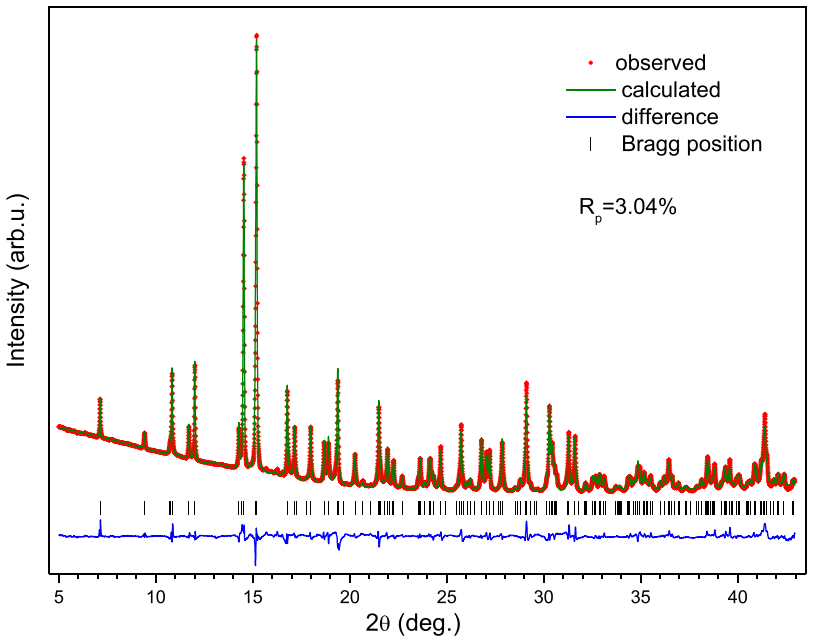

Figure 3. SR XRD pattern of CeMgSnH collected with a multipurpose diffractometer at BM01, SNBL, ESRF, Grenoble, France, using a wavelength of 0.75334 Å. R_{prof} = 0.0304. The vertical bars in the row below the pattern indicate the positions of the Bragg reflections used to calculate the refined pattern. Shown below is the difference between the observed and refined patterns.

the first step of H evolution from CeH_3 (344 °C) when CeH_3 converts to CeH_2 because H atoms are evolved from the octahedral Ce_6 coordinated sites.[33] For comparison, Figure 2 also contains TDS traces for the chemically related CeNiSnH (TiNiSi-type, this work) and MgH_2 synthesized by the RBM of Mg in hydrogen at a pressure of 30 bar H_2. CeNiSnH has a peak of hydrogen evolution at 295 °C, while MgH_2 shows a peak at 302 °C. As the peaks of hydrogen desorption from the tetrahedral Ce_3Ni interstitial sites (CeNiSnH; 295 °C), Mg_4 (MgH_2; 302 °C) are found at lower temperatures as compared to CeMgSnH (peak @ 345 °C) while desorption of hydrogen proceeds at higher temperatures for CeH_2 (H in Ce_4; 655 °C), it can be assumed that hydrogen atoms adopt a mixed Ce + Mg surrounding in the crystal structure of CeMgSnH.

3.3. Crystal and Magnetic Structures of CeMgSnD from SR XRD and NPD Studies at 298 and 2 K. The plot of the Rietveld refinement of the SR XRD pattern of CeMgSnH is displayed in Figure 3. The refinement (R_p = 0.0304) proves the formation of a single-phase TiNiSi-type hydride with the following lattice parameters: space group *Pnma*, a = 8.0700(2) Å; b = 4.47433(8) Å; c = 9.1716(2) Å and V = 331.167(8) Å^3. The hydrogenation/deuteration does not change the TiNiSi structure type. Hydrogen absorption is accompanied by a slight volume expansion of 1.27% (see Table 1). The unit cell expansion mostly proceeds along the [100] direction, i.e., 4.30%. At the same time, the lattice expansion appears to be very small along [001] (0.92%), while the unit cell contracts along [010] (−2.04%).

An indexing of the neutron powder diffraction pattern of the monodeuteride CeMgSnD proves that the TiNiSi-type crystal structure remains unaltered on deuteration. The refinement of the NPD pattern (see Figure 4; R_p = 0.0401) indicated that the D atoms fill half of the Ce_3Mg tetrahedral interstices (one 4*c* site). The crystal structure data of CeMgSnD are compiled in Table 1. A plot of the crystal structure of CeMgSnD is shown in Figure 5. The D-occupied Ce_3Mg tetrahedra are connected

Table 1. Crystal Structure Data of CeMgSnD from a Combined Refinement of SR XRD and NPD Data Collected at 298 K[a,b]

	x	*y*	*z*	B_{iso} (Å^2)
Ce	−0.0159(2)	1/4	0.6680(2)	0.50(2)
Mg	0.3403(2)	1/4	0.4307(2)	0.62(2)
Sn	0.2062(2)	1/4	0.11999(9)	0.53(1)
D	0.0721(2)	1/4	0.42771(8)	1.72(2)

[a]Space group *Pnma* (No. 62). R_p = 3.04%; R_{wp} = 3.45%; R_I = 4.58%; GOF = 1.28. [b]a = 8.0700(2) Å; b = 4.47433(8) Å; c = 9.1716(2) Å; V = 331.167(8) Å^3. All atoms occupy Wyckoff sites 4*c*.

by vertices and edges and form slabs, which proceed parallel to the (*yz*) plane and are stacked along [100].

In CeMgSnD, one-half of the available Ce_3Mg tetrahedral voids are occupied by D atoms in an ordered way. Complete filling of the La_3Ni voids was observed in the related phase $LaNiSnD_2$.[13]

In the D@Ce_3Mg tetrahedra, the metal−D distances are Mg−D, 2.165(2) Å; Ce−D, 2.316(2) Å; and Ce−D, 2 × 2.4456(7) Å. These distances are typical for bonding interactions Mg−H and Ce−H. Since the shortest Sn−D distances are very large, (2.986(2); 3.022(1) Å), Sn and D do not show bonding interactions.

CeMgSnD and LaMgSnD[14] are isostructural; however, due to the lanthanide contraction, the volume of the unit cell of CeMgSnD is significantly reduced (∼3.6%) as compared to the unit cell of LaMgSnD.

Hydrogenation causes a conversion of the antiferromagnetic CeMgSn into ferromagnetic CeMgSnH. From the analysis of the NPD pattern at 298 K and at 2 K, we conclude that the magnetic structure has a propagation vector **k** = [000]. The symmetry analysis shows that this magnetic structure can be described with irreducible representation Γ_3, where the ferromagnetic mode Fy (++++) along the *c*-axis coexists with an antiferromagnetic Gx mode (+−+−) mode along the *a*-axis.

https://doi.org/10.1021/acs.chemmater.4c01104
Chem. Mater. 2024, 36, 6257−6268

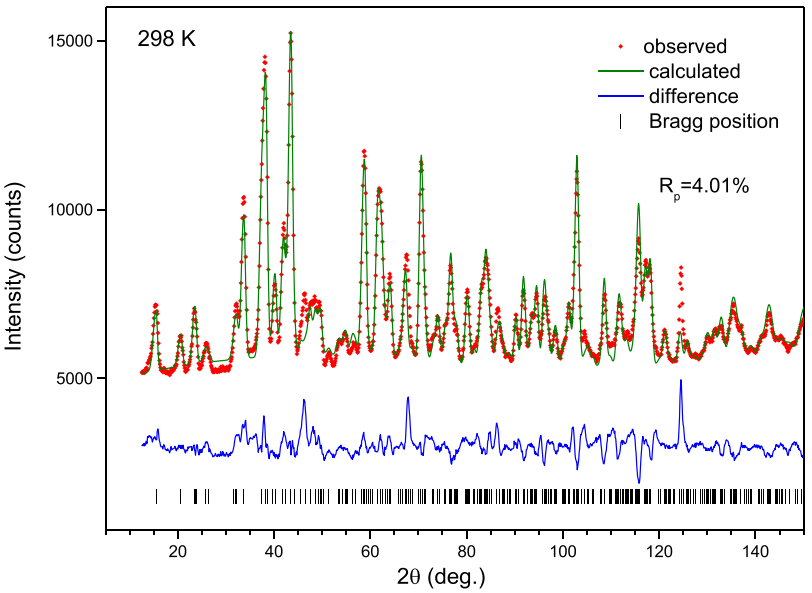

Figure 4. Rietveld refinement of the NPD pattern of CeMgSnD collected at 298 K using the PEARL diffractometer at a wavelength of 1.67 Å at the TU Delft Reactor. The blue line shows the difference between the measured and refined powder patterns, and the vertical bars below mark the angles of the Bragg reflections used to calculate the refined pattern. Several profile functions have been tested during the refinements. Only the pseudo-VOIGT profile function allowed us to adequately refine the data providing a good fit.

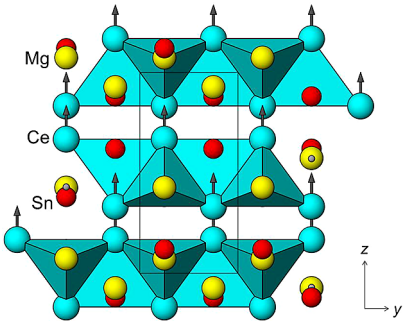

Figure 5. Crystal and magnetic structures of CeMgSnD shown as a projection along [100]. The rows occupied by H/D edge-sharing Ce_3Mg tetrahedra are highlighted in cyan. Orientation of magnetic moments of Ce in the ferromagnetic structure of CeMgSnD along [100] is shown by arrows.

Although the unit cell of the magnetic structure is described by the same unit cell as the crystallographic unit cell, its symmetry allows appearance of extra peaks as compared to the nuclear structure, as can be seen from the calculated Bragg positions of the magnetic peaks (top ticks in Figure 6) as compared to the nuclear peaks (bottom ticks in Figure 6). The main signature of the appearance of the antiferromagnetic modes is the presence of the 001 and 003 reflections. Unfortunately, the reflection 001 is out of the measured angular range of the NPD data, while there is no indication for the presence of the 003 reflection.

The results of refinements of the NPD data collected at 2 K (R_{magn} = 17.5%) are listed in Table 2, while the Rietveld plot is shown in Figure 6. These refinements showed the absence of the contributions from the AFM mode in the neutron diffraction pattern. Rietveld refinements showed that the aligned along [001] direction of the unit cell magnetic moments of Ce atoms have a magnitude of 1.4(3) μ_B.

Cooling from 298 to 2 K caused an isotropic volume contraction by 1.6%.

3.4. Computational Studies of the CeMgSn-H_2 System.

Computational studies of CeMgSn and hydrides in the CeMgSn-H_2 system showed that the most themodynamically favorable is the monohydride CeMgSnH (see Figure 7).

Both CeMgSn and CeMgSnH are magnetically ordered, with the magnetic moment slightly decreasing from 1.4 μ_B (CeMgSn) to 1.0 μ_B (CeMgSnH). In contrast, in $CeMgSnH_2$, the Ce ion does not carry a magnetic moment, while this hydride is less thermodynamically favorable as compared to $CeMgSnH_2$.

The total and site-projected electronic density of states (DOS) at the equilibrium volumes for CeMgSn and for the monohydride CeMgSnH are presented in Figure 8A,B. In addition, the orbital-projected DOS for all phases are shown in Figure 9A,B. In CeMgSnH, the H, Ce, Mg, and Sn hybrid states peak between −6 and −4 eV and exhibit a significant localization tendency, which is more pronounced compared to that of CeMgSn. It is interesting that Sn indirectly engages in the chemical bonding with H, even though there are no direct atomic Sn−H contacts.

The calculated valence electron charge density distributions for CeMgSn and CeMgSnH are displayed in Figure 10. Both phases show a combination of different bonding characteristics—covalent and slightly ionic bonding between the constituent elements. Consequently, there is some degree of charge transfer between the electropositive elements (Ce and Mg) and the more electronegative Sn in CeMgSn. Delocalized Ce and Mg electrons contribute to metallic bonding. Slight covalent bonding between Mg and Sn and Ce and Sn is indicated by electron sharing (see Figure 10).

Insertion of H into CeMgSn significantly alters the bonding nature. Hydrogen occupying interstitial sites in Ce_3Mg tetrahedra within the CeMgSn structure carries a slight negative charge of −0.26 *e*. As there is a strong tendency for hydrogen to attract electrons from the electropositive elements like Mg, the presence of hydrogen can affect the covalent bonding between Mg and Sn and between Ce and Sn. From

https://doi.org/10.1021/acs.chemmater.4c01104
Chem. Mater. 2024, 36, 6257−6268

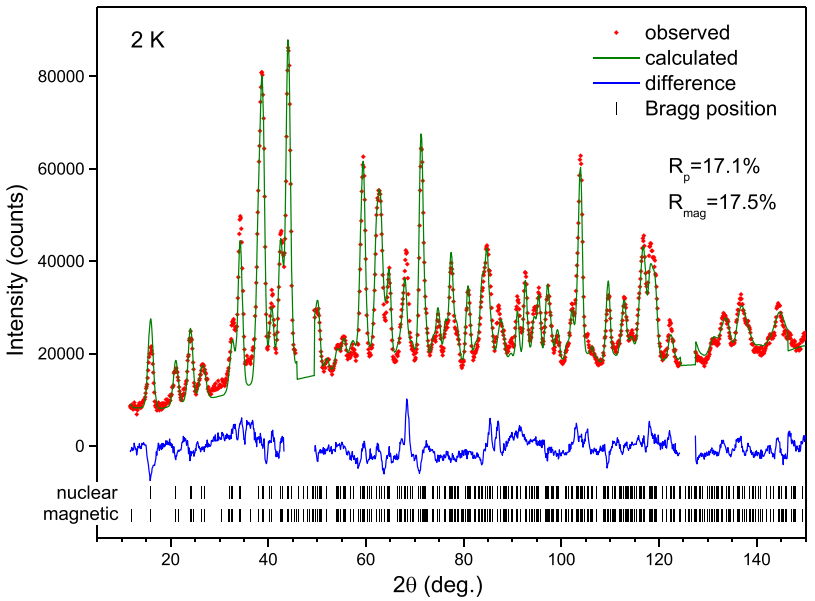

Figure 6. Rietveld refinements of the neutron powder diffraction pattern of CeMgSnD collected at 2 K using a PEARL diffractometer at the TU Delft Reactor with a wavelength of 1.67 Å. R_p: 17.1; R_{wp} 18.2; R_{mag}: 17.5. Positions of the Bragg peaks are shown by ticks. Top: magnetic peaks for CeMgSnD. Bottom: nuclear peaks for CeMgSnD. Excluded regions around 49° and around 128°: contributions from the cryostat.

Table 2. Crystal and Magnetic Structures Data of CeMgSnD Obtained from a Refinement of NPD Data Collected at 2 K (Space Group *Pnma*)[a]

	x	*y*	*z*	B_{iso} (Å^2)
Ce	−0.01819	1/4	0.66756	1.11
Mg	0.33585	1/4	0.42672	1.20
Sn	0.20687	1/4	0.11988	0.95
D	0.07445	1/4	0.42958	2.64

[a] a = 8.0277 Å; b = 4.4539 Å; c = 9.1362 Å; V = 326.6569 Å^3; μ_{Ce} = 1.4(3) μ_B along [001]. All atoms occupy Wyckoff sites 4*c*.

the data listed in Table 3, we conclude that the calculated magnetic moment on the Ce atoms decreases from 1.92 to 1.32 μ_B for CeMgSn and CeMgSnH, respectively, consistent with the experimental findings.

3.5. Magnetization Measurements. Figure 11 displays the inverse magnetic susceptibilities of CeMgSn and CeMgSnD. The susceptibilities exhibit substantial magnetic field dependence. The susceptibilities converge for increasing magnetic fields, suggesting that the field dependence originates from slight ferromagnetic impurities, which can be saturated by sufficiently high magnetic fields. To map out the paramagnetic contribution, a correction for the ferromagnetic impurities was carried out employing the Honda−Owen method, suggesting

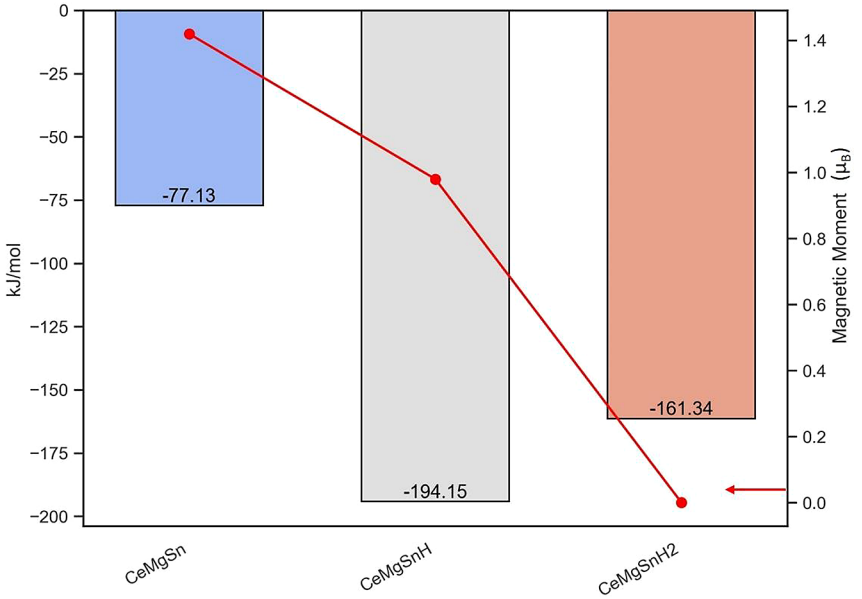

Figure 7. Calculated formation energy at 0 K (ΔH, in the left side) and magnetic moment at the Ce site (in μ_B, in the right-hand side of the axis) for CeMgSn, CeMgSnH, and $CeMgSnH_2$.

https://doi.org/10.1021/acs.chemmater.4c01104
Chem. Mater. 2024, 36, 6257−6268

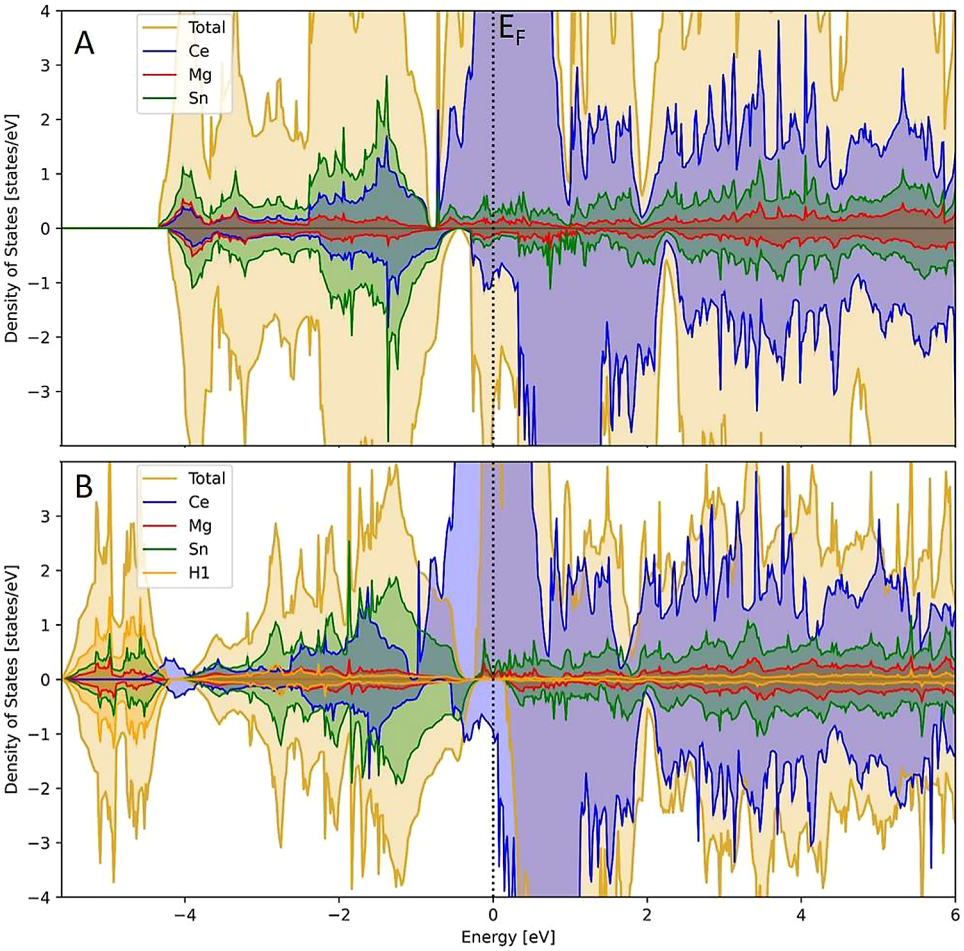

Figure 8. Calculated total and site projected electronic density of states (DOS) for (A) CeMgSn and (B) CeMgSnH. The Fermi energy (E_F) is marked by a vertical dotted line.

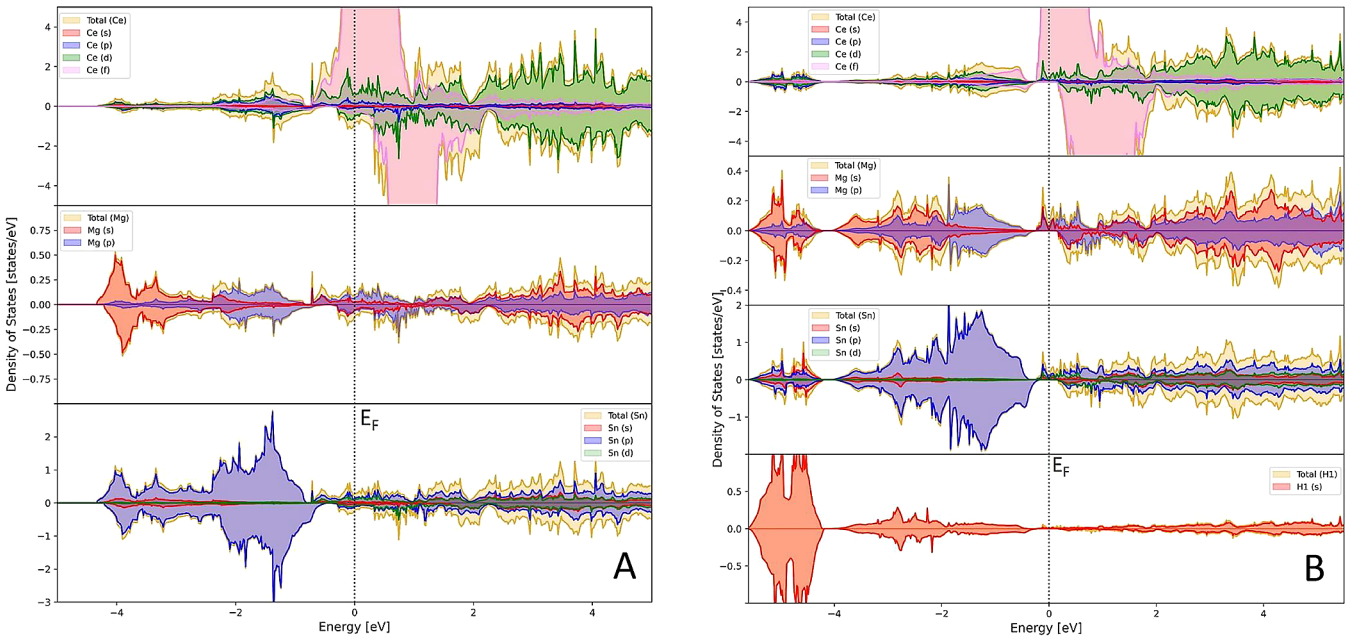

Figure 9. (A) Calculated atom and orbital projected density of states (DOS) for CeMgSn. The Fermi energy (E_F) is marked by a vertical dotted line. (B) Calculated atom and orbital projected density of states (DOS) for CeMgSnH. The Fermi energy (E_F) is marked by a vertical dotted line.

https://doi.org/10.1021/acs.chemmater.4c01104
Chem. Mater. 2024, 36, 6257−6268

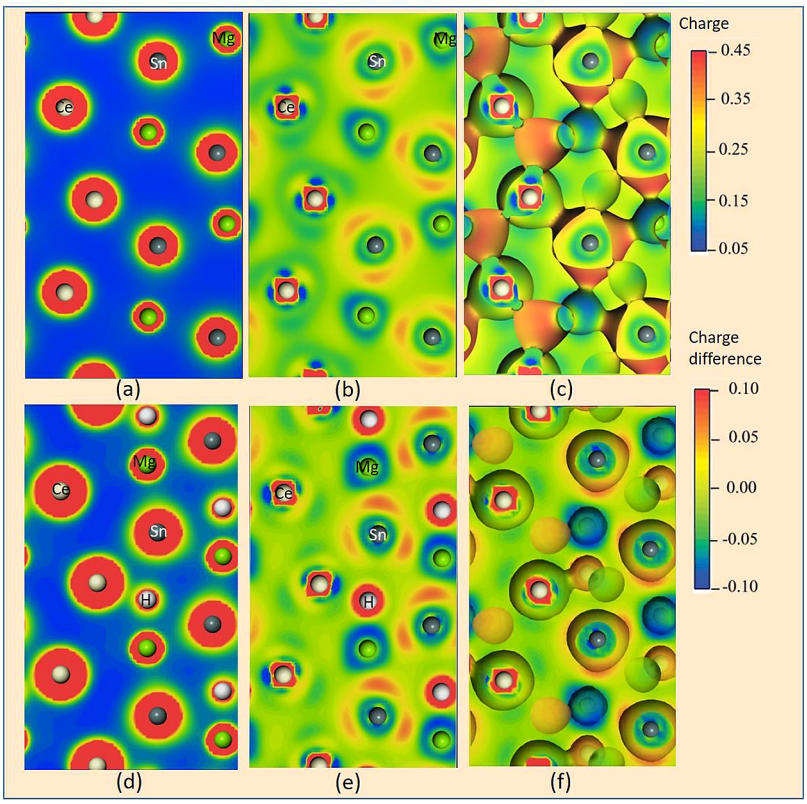

Figure 10. Calculated valence electron charge density distribution (a and d), the charge difference plot (b and e), and the three-dimensional charge transfer distribution (c and f) for CeMgSn (top) and CeMgSnH (bottom).

Table 3. Charge Transfer Characteristics and Calculated Magnetic Moment (in μ_B) among the Different Constituents in CeMgSn and CeMgSnH

compounds	atoms	magnetic moments	charge (in *e*)
CeMgSn	Ce	1.92	+0.44
	Mg	0.04	+0.37
	Sn	0.02	−0.81
CeMgSnH	Ce	1.32	+0.70
	Mg	0.03	+0.17
	Sn	0.02	−0.61
	H	0.02	−0.26

the extrapolation $\mu_0 H \rightarrow \infty$ and full saturation of the ferromagnetic impurity magnetism.[34]

Above ∼150 K, the thus extrapolated susceptibilities follow the Curie−Weiss law

$$\chi_{mol}(T) = \frac{C}{T - \theta_{CW}} + \chi_0 \quad (1)$$

with a Curie−Weiss temperature θ_{CW} and the Curie−Weiss constant C given by

$$C = \frac{N_A p_{eff}^2 \mu_B^2}{3k_B} \quad (2)$$

N_A and k_B are the Avogadro and the Boltzmann constants, respectively. The effective magnetic moment, p_{eff}, is defined as

$$p_{eff} = g_J \sqrt{J(J+1)} \quad (3)$$

with g_J being the Landé *g*-factor.

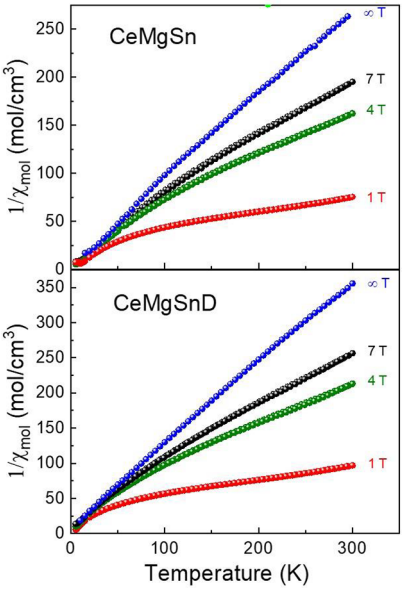

Figure 11. Inverse magnetic susceptibilities of CeMgSn and CeMgSnD as a function of temperature measured at various external magnetic fields, as indicated. The blue circles represent the magnetic susceptibilities obtained by an extrapolation to $\mu_0 H \rightarrow \infty$ (Honda−Owen extrapolation).

Neglecting substantial crystal electric field effects at high temperatures and presuming Russel−Saunders coupling, one expects for Ce in the oxidation state +3 with $g_J = 6/7$ and $J = 5/2$ an effective moment of $\mu_{eff} = 2.54$. χ_0 comprises temperature-independent susceptibility contributions arising

https://doi.org/10.1021/acs.chemmater.4c01104
Chem. Mater. 2024, 36, 6257−6268

from the diamagnetic susceptibility of the electrons in the closed electron shells and a possible Pauli susceptibility contribution in case of a metallic system.[35] The diamagnetic susceptibilities of CeMgSn and CeMgSnD were calculated to be -45×10^{-6} cm^3 mol^{-1} by summing up Pascal's increments for the constituents in their respective oxidation state, as listed by Bain and Berry.[36]

Figure 12 shows the inverse magnetic susceptibilities of CeMgSn and CeMgSnD after Honda–Owen extrapolation

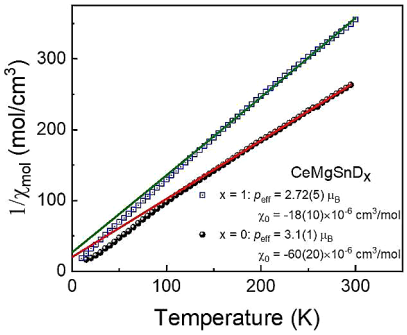

Figure 12. Inverse magnetic susceptibilities of CeMgSn and CeMgSnD with fits of a Curie–Weiss law (eq 1) to the data above ~150 K (solid red and green lines). Fit results are listed in the inset.

with fits of the Curie–Weiss law (eq 1) to the data for $T \geq 150$ K. The effective moments amount to 3.1(1) and 2.72(7) μ_B for CeMgSn and CeMgSnD, respectively. Whereas the effective moment of CeMgSnD only slightly exceeds the expected effective moment of 2.54 μ_B,[36] that of CeMgSn is noticeably larger. Whether this deviation is due to an insufficient correction of ferromagnetic impurities or crystal field splitting effects deserves clarification in forthcoming investigations.

Below ~150 K deviations from the Curie–Weiss law are seen, which can be tentatively ascribed to crystal electric field splitting effects. The fits of the high-temperature susceptibilities result in Curie–Weiss temperatures of −25(2) K. As the isothermal magnetization data indicate (see Figure 13),

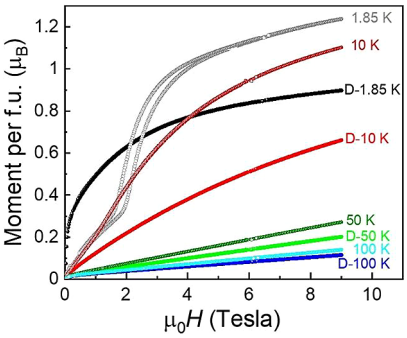

Figure 13. Comparison of the magnetic moments per formula unit (f.u.) of CeMgSn and CeMgSnD as a function of the magnetic field at various temperatures, as indicated.

magnetic ordering occurs below ~10 K and consequently spin exchange contributions to the Curie–Weiss temperature are small and the essential contribution to the Curie–Weiss temperature results from crystal field splitting effects on the susceptibilities.

The temperature-independent contributions, χ_0, to the susceptibilities amount to $-18(10) \times 10^{-6}$ and $-60(20) \times 10^{-6}$ cm^3 mol^{-1} for CeMgSnD and CeMgSn, respectively, indicating essential Pauli susceptibility contributions in case of CeMgSnD only.

Figure 13 displays the results of the isothermal magnetization measurements. They revealed marked differences between the two compounds. Whereas CeMgSnD shows paramagnetism with Brillouin-type saturation behavior at 1.85 K, CeMgSn exhibits a field dependence, reminiscent of the magnetization dependence of an antiferromagnet with easy axis anisotropy revealing a spin-flop like jump of the magnetization at ~2 T. At 10 K and above, the magnetization shows a Brillouin-like field dependence. The saturated moment of CeMgSn approaches 1.25 μ_B, while the magnetization of CeMgSnD tends to saturation with a moment of ~0.9 μ_B, both significantly reduced when compared with the theoretical value for Ce^{3+} of 2.14 μ_B according to $g \times J$.[37] The substantially reduced saturation moment maybe attributed to a crystal field splitting of the $J = 5/2$ ground state of the Ce^{3+} ions. Similar behavior has been observed for many of the equiatomic CeTX compounds.[6,7,38]

The magnetic ordering behavior of CeMgSn and CeMgSnD in the low-temperature regime was studied by zero-field-cooled (ZFC)/field-cooled (FC) measurements with a low field strength of 100 Oe (Figure 14). CeMgSn shows long-range

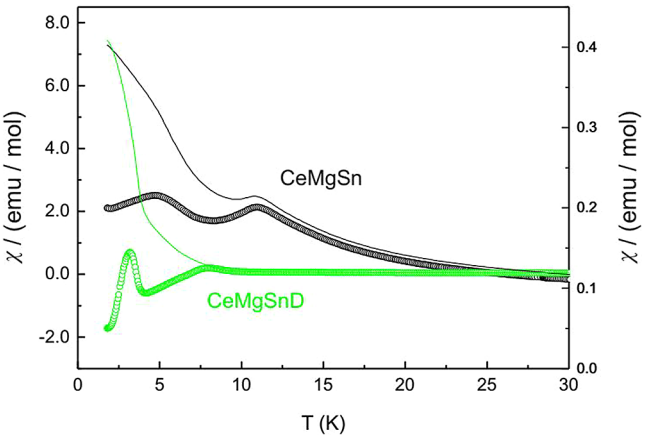

Figure 14. Temperature dependence of the zero-field-cooled (circles) and field-cooled (lines) magnetic susceptibilities of CeMgSn and CeMgSnD measured at 100 Oe.

antiferromagnetic ordering below T_N = 10.9(1) K, in agreement with the previous studies by Lemoine et al., who reported antiferromagnetic ordering below 12 K.[39] An antiferromagnetic ground state is supported by the metamagnetic behavior in the 1.85 K magnetization isotherm (Figure 13).

For the deuterated sample, we observe a decrease of the magnetic ordering temperature and a change of the magnetic ground state. CeMgSnD shows a strong increase of the susceptibility in the FC plot (Figure 14), indicating ferromagnetic ordering (consistent with the neutron diffraction experiments). The transition is fairly broad, probably a consequence of the small homogeneity range $CeMgSnD_{1-x}$ and the distribution of domains with slightly different Curie temperatures. A ferromagnetic ground state is corroborated by the 1.85 K magnetization isotherm. We do not see typical signs of a soft magnetic material behavior since the magnetization

https://doi.org/10.1021/acs.chemmater.4c01104
Chem. Mater. 2024, 36, 6257−6268

increase proceeds over the whole field range, and we still do not see saturation at 90 kOe.

3.6. ^{119}Sn Mössbauer Spectroscopy. The ^{119}Sn Mössbauer spectra of CeMgSn and its monohydride CeMgSnD taken at 78 K are presented in Figure 15. They

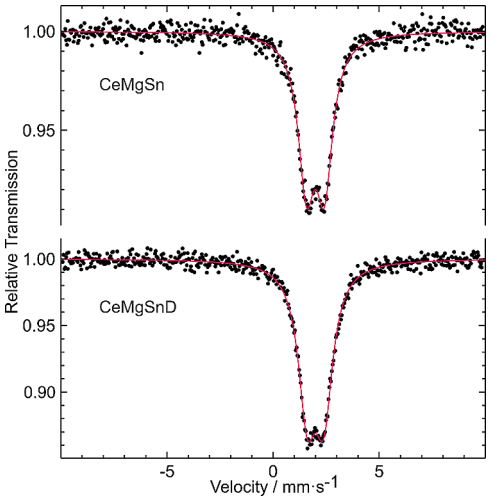

Figure 15. Experimental (dots) and simulated (red lines) ^{119}Sn Mössbauer spectra of CeMgSn (top) and CeMgSnD (bottom) measured at 78 K.

could be well reproduced with single signals at isomer shifts of 1.99(1) and 2.00(1) mm s^{-1}, respectively. This is in excellent agreement with the single Sn sites determined from the diffraction data. The calculated charge transfer (Table 3) indicated a slight charge change for the tin atoms from −0.81 for CeMgSn to −0.61 for CeMgSnH, compatible with a small oxidation of the tin atoms. However, this small change is not evident from the experimental ^{119}Sn spectra. The isomer shifts of CeMgSn and CeMgSnD (Figure 15 and Table 4) are identical within one standard deviation. The hydrogenation process thus induces only a negligible change in the electron density at the tin nuclei.

Table 4. Fitting Parameters of the ^{119}Sn Mössbauer Spectroscopic Measurements of CeMgSn and CeMgSnD at 78 K[a]

compound	δ/mm s^{-1}	ΔE_Q/mm s^{-1}	Γ/mm s^{-1}
CeMgSn	1.99(1)	0.85(1)	0.95(2)
CeMgSnD	2.00(1)	0.78(1)	1.03(1)

[a] δ = isomer shift, ΔE_Q = quadrupole splitting, and Γ = experimental line width.

The quadrupole splitting parameters of 0.85(1) and 0.78(1) mm s^{-1} reflect the noncubic site symmetry (*.m.*) of the tin atoms (see Table 4).

LaMgSn and its hydride LaMgSnH were recently investigated by ^{119}Sn Mössbauer spectroscopy.[14] The comparison of the isomer shift and quadrupole splitting values of CeMgSn and its monohydride with the corresponding lanthanum phases (LaMgSn: δ = 1.98(2) mm s^{-1}, ΔE_Q = 0.93(1) mm s^{-1}; LaMgSnH: 1.99(1) mm s^{-1}, ΔE_Q = 0.82(1) mm s^{-1}) suggest similar *s* electron density distribution in the cerium and lanthanum phases. Since the hydrogen atoms in LaMgSnH and CeMgSnH have tetrahedral H@La$_3$Mg and H@Ce$_3$Mg coordination and there are no direct tin−hydrogen interactions, the tin atoms are only marginally affected by the hydrogenation process.

4. CONCLUDING REMARKS

CeMgSn was initially studied with respect to its potential for precipitation hardening in Mg−Sn−Zn alloys.[40−42] Herein, we investigated the hydrogenation behavior of CeMgSn and the properties of monohydride CeMgSnH(D). We find that formation of the monohydride is favored rather than the decomposition into the binary hydrides of Mg and Ce. The metal substructure, orthorhombic TiNiSi type, remains unaltered on hydrogenation. CeMgSn shows a hydrogen storage capacity of 1 at.H/f.u., similar to LaMgSnH. The dihydride CeMgSnH$_2$ can possibly be formed by filling all available Ce$_3$Mg tetrahedral voids by H atoms. Electronic structure calculations reveal that tin creates strong bonds with the surrounding Ce and Mg atoms forming tricapped trigonal prisms [Sn@Mg$_4$Ce$_5$].[43] Replacing La by Ce in the intermetallic phases REMgSn causes a 3.6% volume contraction for both intermetallic and corresponding hydride structures, caused by the smaller size of the Ce atoms as compared to the La atoms. Magnetic susceptibility and magnetization studies indicate a transition from antiferromagnetism in CeMgSn to ferromagnetism in CeMgSnH. ^{119}Sn Mössbauer spectra indicate almost similar electron density at the tin nuclei of CeMgSn and CeMgSnH and parallel the results for the pair LaMgSn/LaMgSnH and other equiatomic stannides CeTSn.[14]

■ ASSOCIATED CONTENT

Supporting Information

The Supporting Information is available free of charge at https://pubs.acs.org/doi/10.1021/acs.chemmater.4c01104.

Crystallographic data for the CeNiSn stannide (PDF)

■ AUTHOR INFORMATION

Corresponding Authors

Volodymyr A. Yartys − *Institute for Energy Technology, Kjeller NO 2027, Norway;* orcid.org/0000-0003-4207-9127; Email: volodymyr.yartys@ife.no

Reinhard K. Kremer − *Max-Planck-Institut für Festkörperforschung, Stuttgart 70569, Germany;* orcid.org/0000-0001-9062-2361; Email: rekre@fkf.mpg.de

Rainer Pöttgen − *Institut für Anorganische und Analytische Chemie, Universität Münster, Münster 48149, Germany;* Email: pottgen@uni-muenster.de

Authors

Lev G. Akselrud − *Department of Inorganic Chemistry, Faculty of Chemistry, Ivan Franko National University of Lviv, Lviv 79005, Ukraine*

Roman V. Denys − *Institute for Energy Technology, Kjeller NO 2027, Norway*

Ponniah Vajeeston − *Center for Materials and Nanotechnology, University of Oslo, Oslo NO 0315, Norway;* orcid.org/0000-0002-5566-2429

Bachir Ouladdiaf − *Institute Laue-Langevin, Grenoble, Cedex 9 38042, France*

Robert Dankelman − *Delft University of Technology (TU Delft), Delft Reactor Intituut, Delft 2629, The Netherlands*

https://doi.org/10.1021/acs.chemmater.4c01104
Chem. Mater. 2024, 36, 6257−6268

Jeroen Plomp − *Delft University of Technology (TU Delft), Delft Reactor Intituut, Delft 2629, The Netherlands*
Aylin Koldemir − *Institut für Anorganische und Analytische Chemie, Universität Münster, Münster 48149, Germany*
Lars Schumacher − *Institut für Anorganische und Analytische Chemie, Universität Münster, Münster 48149, Germany;* orcid.org/0009-0009-9444-8773
David S. Wragg − *Institute for Energy Technology, Kjeller NO 2027, Norway*
Bruno Guilherme Fischer Eggert − *Institute for Energy Technology, Kjeller NO 2027, Norway*
Vasyl Berezovets − *Institute for Energy Technology, Kjeller NO 2027, Norway*

Complete contact information is available at: https://pubs.acs.org/10.1021/acs.chemmater.4c01104

Author Contributions

The manuscript has been jointly prepared by all coauthors, V.A.Y., L.G.A., R.V.D., P.V., B.O., R.D., J.P., A.K., L.S., R.K.K., R.P., D.W., B.G.F.E., and V.B., who reviewed and approved its content.

Notes

The authors declare no competing financial interest.

■ ACKNOWLEDGMENTS

This paper is a part of a Virtual Special Issue of Chemistry of Materials dedicated to the memory of Professor Francis J. DiSalvo. This work has received a support from the EU Horizon 2020 programme in the frame of the H2020-MSCA RISE-2017 action, HYDRIDE4MOBILITY project, with Grant Agreement 778307 (V.A.Y., R.V.D., and V.B.). V.A.Y. acknowledges the support from the Institute for Energy Technology. A part of this research was funded by Universität Münster and Deutsche Forschungsgemeinschaft (INST 211/1034-1). The authors appreciate the possibility to collect the SR XRD data at BM01, SNBL, ESRF, Grenoble, France, and NPD data at Delft Reactor Institute, TU Delft, The Netherlands. We thank E. Brücher from MPI-FKF for part of the magnetic measurements.

■ REFERENCES

(1) Villars, P.; Cenzual, K. *Pearson's Crystal Data: Crystal Structure Database for Inorganic Compounds (release 2022/23)*; ASM International®: Materials Park, Ohio, 2022.
(2) Szytuła, A., Leciejewicz, J. *Handbook of Crystal Structures and Magnetic Properties of Rare Earth Intermetallics*; CRC Press: Boca Raton, 1994.
(3) Matar, S. F. Intermetallic hydrides: A review with ab initio aspects. *Prog. Solid State Chem.* **2010**, *38*, 1−37.
(4) Gingl, F.; Yvon, K.; Vogt, T.; Hewat, A. Synthesis and crystal structure of tetragonal $LnMg_2H_7$ (Ln = La, Ce), two Laves phase hydride derivatives having ordered hydrogen distribution. *J. Alloys Compd.* **1997**, *253*−*254*, 313−317.
(5) Yang, F.; Wang, J.-W.; Ke, J.-L.; Pan, Z.-G.; Tang, B.-Y. Elastic properties and electronic structures of Mg−Ce intermetallic compounds from first-principles calculations. *Phys. Status Solidi B* **2011**, *248*, 2097−2102.
(6) Pöttgen, R.; Janka, O.; Chevalier, B. Cerium intermetallics CeTX − review III. *Z. Naturforsch.* **2011**, *71b*, 165−191.
(7) Janka, O.; Niehaus, O.; Pöttgen, R.; Chevalier, B. Cerium intermetallics with TiNiSi-type structure. *Z. Naturforsch.* **2016**, *71*, 737−764.
(8) Yartys, V. A.; Ouladdiaf, B.; Isnard, O.; Khyzhun, Yu. O.; Buschow, K. H. J. Hydrogen induced antiferromagnetism in the Kondo semimetal CeNiSn. *J. Alloys Compd.* **2003**, *359*, 62−65.
(9) Chevalier, B.; Bobet, J. L.; Pasturel, M.; Bauer, E.; Weill, F.; Decourt, R.; Etourneau, J. Ferromagnetic Behavior of the New Hydride $CeNiSnH_{1.8(2)}$. *Chem. Mater.* **2003**, *15*, 2181−2185.
(10) Chevalier, B.; Bobet, J. L.; Gaudin, E.; Pasturel, M.; Etourneau, J. The Ternary Gallide CeNiGa: Polymorphism and Hydrogen Absorption. *J. Solid State Chem.* **2022**, *168*, 28−33.
(11) Chevalier, B.; Wattiaux, A.; Bobet, J. L. The Doniach diagram and hydrogenation of the ternary compounds CePdIn and CePdSn. *J. Phys.: Condens. Matter.* **2006**, *18*, 1743−1755.
(12) Chevalier, B.; Decourt, R.; Heying, B.; Schappacher, F. M.; Rodewald, U. Ch.; Hoffmann, R. D.; Pöttgen, R.; Eger, R.; Simon, A. Inducing Magnetism in the Kondo Semiconductor CeRhSb through Hydrogenation: Antiferromagnetic Behavior of the New Hydride $CeRhSbH_{0.2}$. *Chem. Mater.* **2007**, *19*, 28−35.
(13) Yartys, V. A.; Olavesen, T.; Hauback, B. C.; Fjellvåg, H.; Brinks, H. W. Hexagonal $LaNiSnD_2$ with a filled ZrBeSi-type structure. *J. Alloys Compd.* **2002**, *330*−*332*, 141−145.
(14) Yartys, V. A.; Denys, R. V.; Akselrud, L. G.; Vajeeston, P.; Dankelman, R.; Plomp, J.; Block, T.; Pöttgen, R.; Wragg, D.; Fischer Eggert, B. G.; Berezovets, V. Structure and bonding in TiNiSi type LaMgSnH intermetallic hydride. *J. Alloys Compd.* **2024**, *976*, No. 173198.
(15) Manfrinetti, P.; Provino, A.; Gschneidner, K. A., Jr. On the RMgSn rare earth compounds. *J. Alloys Compd.* **2009**, *482*, 81−85.
(16) Ritter, C.; Provino, A.; Manfrinetti, P.; Gschneidner, K. A., Jr. The magnetic structures of RMgSn compounds (R = Ce, Pr, Nd, Tb). *J. Alloys Compd.* **2011**, *509*, 9724−9732.
(17) Suwarno, S.; Lototskyy, M. V.; Yartys, V. A. Thermal desorption spectroscopy studies of hydrogen desorption from rare earth metal trihydrides REH_3 (RE = Dy, Ho, Er). *J. Alloys Compd.* **2020**, *842*, No. 155530.
(18) Dyadkin, V.; Pattison, P.; Dmitriev, V.; Chernyshov, D. A new multipurpose diffractometer PILATUS@SNBL. *J. Synchr. Rad.* **2016**, *23*, 825−829.
(19) van Eijck, L.; Cussen, L. D.; Sykora, G. J.; Schooneveld, E. M.; Rhodes, N. J.; van Well, A. A.; Pappas, C. Design and performance of a novel neutron powder diffractometer: PEARL at TU Delft. *J. Appl. Crystallogr.* **2016**, *49*, 1398−1401.
(20) Akselrud, L.; Grin, Yu. WinCSD: software package for crystallographic calculations (Version 4). *J. Appl. Crystallogr.* **2014**, *47*, 803−805.
(21) Rodríguez-Carvajal, J. Recent advances in magnetic structure determination by neutron powder diffraction. *Phys. B Phys. Condens. Matter.* **1993**, *192*, 55−69.
(22) *ORIGINPRO 2016G (version 9.3.2.303)*; OriginLab Corp.: Northampton, MA, 2016.
(23) *CorelDRAW Graphics Suite 2017 (version 19.0.0.328)*; Corel Corporation: Ottawa, ON, 2017.
(24) Brand, R. A. *WinNormos for Igor6 (version for Igor 6.2 or above: 22/02/2017)*; Universität Duisburg: Duisburg, 2017.
(25) Long, G. J.; Cranshaw, T. E.; Longworth, G. The ideal Mössbauer effect absorber thickness. *Moessbauer Eff. Ref. Data J.* **1983**, *2*, 42−49.
(26) Kresse, G.; Marsman, M.; Furthmuller, J. *VASP the GUIDE; VASP Man, Vienna Ab-Initio Package Vienna Simulation*, 2014; p 237.
(27) Sun, G.; Kürti, J.; Rajczy, P.; Kertesz, M.; Hafner, J.; Kresse, G. Performance of the Vienna ab initio simulation package (VASP) in chemical applications. *J. Mol. Struct.* **2003**, *624*, 37−45.
(28) Hohenberg, P.; Kohn, W.; Kohn, W. Inhomogeneous electron gas. *Phys. Rev.* **1964**, *136*, B864.
(29) Kohn, W.; Sham, L. J. Self-Consistent Equations Including Exchange and Correlation Effects. *Phys. Rev.* **1965**, *140*, A1133.
(30) Perdew, J. P.; Burke, K.; Ernzerhof, M. Generalized Gradient Approximation Made Simple. *Phys. Rev. Lett.* **1996**, *77*, 3865−3868.

(31) Kresse, G.; Joubert, D. From Ultrasoft Pseudopotentials to the Projector Augmented-Wave Method. *Phys. Rev. B: Condens. Matter Mater. Phys.* **1999**, *59*, 1758−1775.
(32) Blöchl, P. E. Projector Augmented-Wave Method. *Phys. Rev. B: Condens. Matter Mater. Phys.* **1994**, *50*, 17953−17979.
(33) Yartys, V. A.; Gutfleisch, O.; Panasyuk, V. V.; Harris, I. R. Desorption characteristics of rare earth (R) hydrides (R = Y, Ce, Pr, Nd, Sm, Gd and Tb) in relation to the HDDR behaviour of R−Fe-based compounds. *J. Alloys Compd* **1997**, *253*−*254*, 128−133. PIIS0925−8388(96)03097−6.
(34) Honda, K. Die thermomagnetischen Eigenschaften der Elemente. *Ann. Phys.* **1910**, *337*, 1027−1063.
(35) Kremer, R. K. Rare Earths Magnetism-Condensed Matter, In *Rare Earth Chemistry*; Pöttgen, R.; Jüstel, Th.; Strassert, C. A., Eds.; de Gruyter STEM: Berlin, 2020; ch 3.3.
(36) Bain, G. A.; Berry, J. F. Diamagnetic Corrections and Pascal's Constants. *J. Chem. Educ.* **2008**, *85*, 532−536.
(37) Lueken, H. *Magnetochemie*; Teubner: Stuttgart, 1999.
(38) Pöttgen, R.; Chevalier, B. Cerium Intermetallics with ZrNiAl-Type Structure − A Review. *Z. Naturforsch.* **2015**, *70b*, 289−304.
(39) Lemoine, P.; Vernière, A.; Marêché, J. F.; Malaman, B. Magnetic properties of the ternary RMgSn (R = Pr, Nd, Sm, Gd-Tm): First series of antiferromagnetic CeScSi-type structure compounds. *J. Alloys Compd.* **2010**, *508*, 9−13.
(40) Hefei Jiuzhou Longteng Scientific and Technological Achievement Transformation Co., Ltd. Chinese Patent CN 113718146 B, 2021.
(41) Yarkadaş, G.; Kumruoğlu, C. L.; Şevik, H. The effect of Cerium addition on microstructure and mechanical properties of high-pressure die cast Mg-5Sn alloy. *Mater. Charact.* **2018**, *136*, 152−156.
(42) Yang, H.; Chai, Y.; Jiang, B.; Yuan, M.; Yang, Q.; Xia, D.; He, J. Simultaneous improvements in strength and ductility of as-extruded Mg-1.0Sn-0.5Zn alloys via Ce addition in combination with pre-twining formation. *J. Alloys Compd.* **2022**, *927*, No. 166879.
(43) Matar, S. F.; Pöttgen, R. Chemical bonding in equiatomic cerium intermetallics − The case of CeMgSn, CePdSn, and CePdMg. *Solid State Sci.* **2015**, *48*, 205−211.

https://doi.org/10.1021/acs.chemmater.4c01104
Chem. Mater. 2024, 36, 6257−6268